Anomalously Large Ground Motion in the 2016 M_L 6.6 Meinong, Taiwan, Earthquake: A Synergy Effect of Source Rupture and Site Amplification

by Shiann-Jong Lee, Te-Yang Yeh, and Yen-Yu Lin

ABSTRACT

On 6 February 2016, an M_L 6.6 earthquake occurred in the Meinong area of southern Taiwan, causing anomalously large ground shaking. In this study, a joint source inversion was performed to understand the rupture process of this event and to identify how the anomalous strong motion was produced. The results show that the rupture process of this event was complex; at least two asperities were identified on the fault plane. The rupture mainly developed in the down-dip direction and propagated toward the northwest. Results from a 3D wave propagation simulation further indicate that the strong ground shaking observed in southwest Taiwan was caused by a combination of three effects: (1) rupture directivity, (2) source radiation pattern, and (3) sedimentary amplification. The results demonstrate that constructive source rupture and wave propagation effects due to a moderate earthquake can cause anomalously strong ground motion and serious seismic hazards in nearby densely populated areas.

Online Material: Figures comparing observed and synthetic waveforms and Global Positioning System (GPS) displacements and spatial–temporal resolution and parameter tests, and movie showing wave propagation.

INTRODUCTION

On the morning of 6 February 2016, at 03:57:26 (UTC +8:00), a moderately large earthquake with a local magnitude of M_L 6.6, named the 0206 Meinong earthquake, struck southern Taiwan. With an $M_L > 6$, this event was the first, as well as the largest, inland earthquake in Taiwan during 2016. The earthquake report released by the Central Weather Bureau (CWB) indicated that the hypocenter was at 120.544° E 22.922° N, with a depth of 14.6 km. It was located in an area

with a complex tectonic background (Yen and Tien, 1986; Deffontaines *et al.*, 1997; Lacombe *et al.*, 2001), where the 2010 Jiashian earthquake (M_L 6.4) had also occurred (Ching *et al.*, 2011; Huang *et al.*, 2011; Lee *et al.*, 2013). Many places in southwestern Taiwan experienced a CWB seismic intensity greater than 5 (80–250 Gal). According to the results of the ground-motion prediction equations (Lin *et al.*, 2011), the estimate of average peak ground acceleration (PGA) of an M_w 6.5 earthquake near the source area is ∼200 Gal. However, extreme cases with a seismic intensity of 7 (> 400 Gal) were recorded by local instruments in Tainan City. Because of the strong ground motion, a considerable amount of building damage was reported. In particular, a high-rise building completely collapsed in Tainan (Fig. 1). In total, this event caused 117 deaths and more than 500 casualties.

This earthquake was clearly recorded by several real-time seismic networks, including the CWB 24-bit Seismic Monitoring Network, the Broadband Array in Taiwan for Seismology (BATS), and *P*alert (Wu *et al.*, 2013). Anomalously large ground motion during the Meinong earthquake was shown by three *P*alert near-field records (Fig. 1). Data recorded at near-field stations with similar epicentral distances (< 25 km) show abrupt changes in waveform characteristics and peak amplitudes. A large peak ground velocity of 101.1 cm/s was recorded at W21B, a station to the west of the epicenter, whereas those recorded at stations to the east were only 13.2 cm/s (at W052) and 4.4 cm/s (at W057). The peak amplitude of the anomalously strong pulse-like velocity waveform recorded at the station to the west (W21B) was at least 20 times larger than those recorded on the eastern side (W057).

Several active faults have been identified around the location of this event as well as in surrounding regions (Fig. 1). However, none of the focal planes shown by the centroid moment tensor (CMT) reports from the CWB or the Global CMT (Dziewonski *et al.*, 1981) match the geometry of the known active faults. All CMT results indicated two fault planes—one
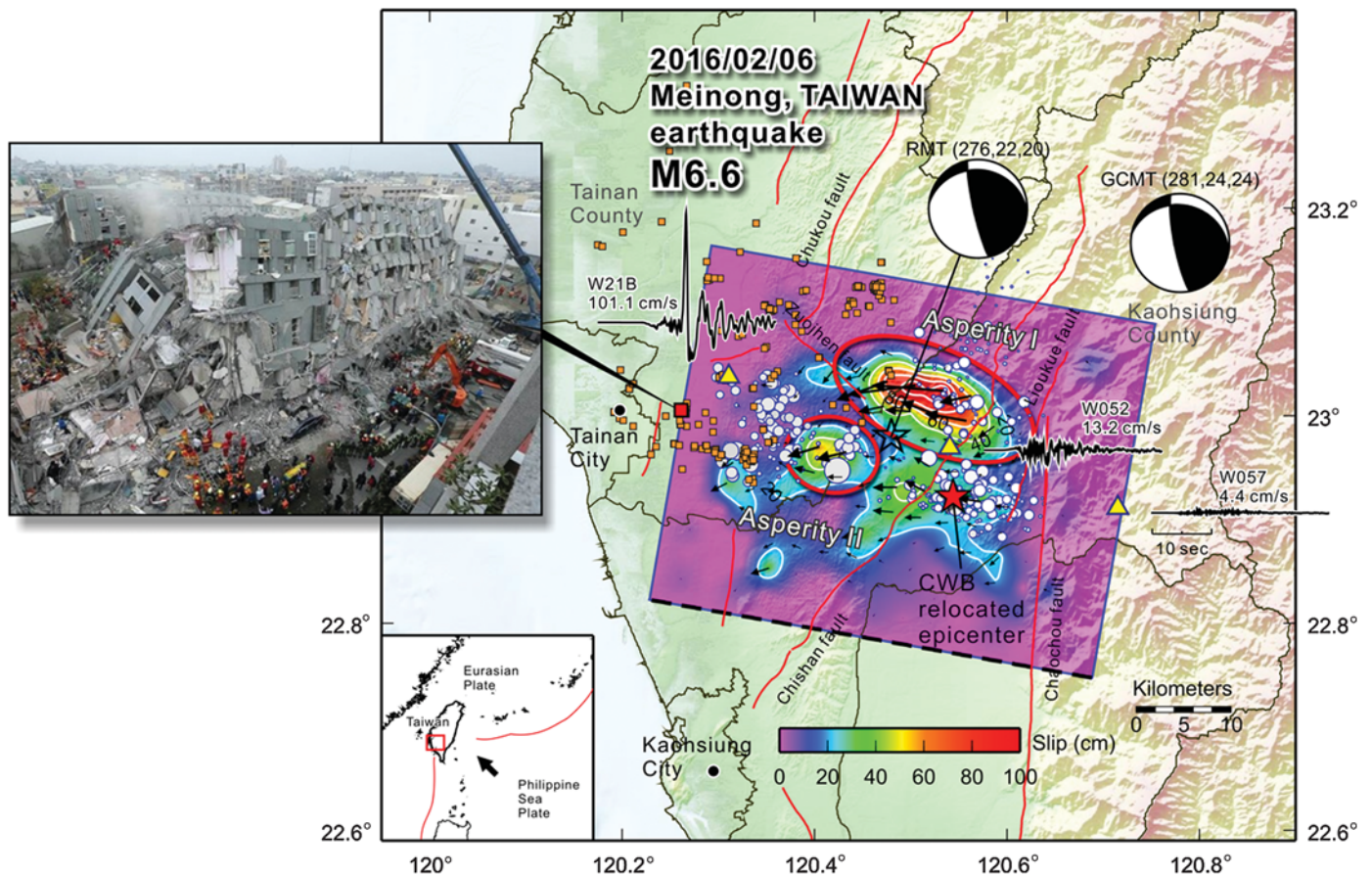
▲ **Figure 1.** Map view of the slip distribution of the 2016 Meinong earthquake. The Central Weather Bureau (CWB) epicenter is indicated with a red star and the real-time moment tensor (RMT) centroid location is shown as an open star. Focal mechanism plots show the focal mechanisms determined by the Global Centroid Moment Tensor (CMT) and RMT. Vectors are the slip direction and the amount of slip on each subfault. Gray circles are the first five days of CWB relocated aftershocks. The active faults in the study area are shown with red lines. Dark yellow squares are the damaged buildings. The inset marks the study region in a larger map of East Asia. The photo in the left shows a fully collapsed high-rise building in Tainan destroyed by the Meinong earthquake.

high-angle thrust fault dipping toward the west and another low-angle strike-slip fault dipping toward the north. The centroid location reported by real-time moment tensor monitoring (Lee *et al.*, 2013) was ~10 km northwest of the CWB epicenter (Fig. 1). There were 362 aftershocks that occurred in the five days after the mainshock, with an M_L ranging from 0.46 to 5.30. Two separate groups of aftershocks were located in the eastern and western portions of the mainshock epicenter. The spatial distribution of aftershock locations roughly formed a northwest–southeast pattern (Fig. 1). It is noted that a gap occurred between these two groups of aftershocks.

To investigate how this event produced strong ground shaking in southern Taiwan, this study developed a numerical earthquake model of the Meinong earthquake. First, we performed a joint inversion to analyze the source rupture process. The inverted source model was then used for the forward spectral-element method (SEM) simulation. In these inverse and forward processes, the 3D path effects are identical because the same regional 3D tomography model was used. Finally,

the rupture process of the Meinong earthquake and its influence on strong ground motion were discussed.

SOURCE RUPTURE PROCESS INVERSION

To investigate the rupture process of the Meinong earthquake, we performed a joint source inversion. Three data sets, including teleseismic body waves, Global Positioning System (GPS) coseismic displacements, and local ground-motion records, were included in the inversion. The seismic waveforms and GPS data that were used are shown in Ⓔ Figures S1–S3 (available in the electronic supplement to this article). Data from 28 teleseismic Incorporated Research Institutions for Seismology stations with epicentral distances ranging between 30° and 90° were used. We deconvolved the instrument response to obtain teleseismic displacement records. The records were subsampled by taking 10 samples every second and filtered to 0.01–1.0 Hz passband. A 42-s time window, starting from 10 s prior to the P arrival, was used. Coseismic GPS displacements were compiled

by the CWB. There were 279 coseismic displacements used in the inversion. Data from three seismic networks were incorporated in the local ground-motion records, including the CWB 24-bit Seismic Monitoring Network, BATS, and *P*alert. For local data, we inverted velocity waveforms with a 35-s time window beginning from the event origin time. The CWB 24-bit and BATS records were subsampled to a 0.1-s sampling rate, and the band-pass filter range was 0.05–0.33 Hz, whereas the *P*alert records were particularly filtered to 0.1–0.33 Hz. It is shown that the local ground-motion data from the combination of the three networks provide good azimuthal coverage surrounding the source area.

The finite-fault source inversion problem is generally formulated in a linear form, $\mathbf{Ax} = \mathbf{b}$ (Hartzell and Heaton, 1983), in which $\mathbf{A}$ is the matrix of Green's functions, $\mathbf{b}$ is the observed data vector, and $\mathbf{x}$ is the solution vector of the slip. We minimized the following objective function using a nonnegative least-squares (NNLS) inversion

$$\min_{x} f(x) = \frac{1}{2}||(\mathbf{Ax} - \mathbf{b})||^2 + \lambda^2||\mathbf{Fx}||^2 \quad \text{subject to } \mathbf{x} \geq 0,$$

(1)

in which $\mathbf{F}$ is the smoothing and damping matrix, and λ is the weighting of linear constraints. If the set of equations $\mathbf{Fx} \sim 0$ has a form such that $\mathbf{x}_i - \mathbf{x}_j \sim 0$, in which i and j are the indexes of adjacent subfaults, then the solution is constrained to have a smoothly varying spatial distribution. In addition, if the $\mathbf{x}_k \sim 0$, in which k is the indexes of subfaults at the fault boundary, then the solution of slip is constrained to diminish at the edge. A misfit function, defined as $(\mathbf{Ax} - \mathbf{b})^2/\mathbf{b}^2$, was used to evaluate the fit of the data. We used a parallel NNLS inversion technique (Lee *et al.*, 2006) to deal with the complex source inversion problem. The number of processors (or CPU cores) depends on the number of time windows used in the inversion. In this study, we considered 60 multiple time windows, and thus 60 CPU cores were deployed for one inversion. The computation was carried out on the Institute of Earth Sciences (IES) Green Cluster, taking about 8.6 min for each run. For the calculation of teleseismic Green's functions, we used the approach developed by Kikuchi and Kanamori (1982). The geodetic Green's functions were calculated based on the analytic expression presented by Okada (1985). For the local ground-motion data, the 3D synthetic Green's functions were calculated based on the SEM (Komatitsch and Tromp, 1999; Komatitsch *et al.*, 2004). In the SEM mesh model, a regional 3D velocity model derived by Huang *et al.* (2014) was incorporated. Details of the SEM mesh model built for the whole of Taiwan are discussed in the Ⓔ electronic supplement (see also Fig. S6). The local synthetic Green's functions were filtered to the same frequency bands applied to the observed data.

Based on the fault-plane solution reported by the Global CMT and the aftershocks reported by the CWB, we considered a fault model with a northwest–southeast strike, dipping to the north (strike 281° and dip 24°). The fault plane was divided into 195 subfaults with a size of 3×3 km^2, resulting in a total fault dimension of 45×39 km^2 (Fig. 1). A maximum rupture

speed of 3.5 km/s was allowed in the inversion. There were 60 time windows with 0.4 s duration, each having 0.2 s overlap between subsequent time windows. This enables each subfault to slip freely within 12.2 s. To ensure the different data sets contributed equally to the inversion, a normalized weight was given in the inversion. The result of the data fittings (Ⓔ Figs. S1–S3) and the two inversion tests (Ⓔ Figs. S4 and S5) are provided in the electronic supplement.

Joint source inversion shows that the slip was distributed across an area with a size of $\sim$25 $\times$ 25 km^2 (Fig. 1). Complex slip distributions with at least two asperities were found on the fault plane. Asperity I was the largest asperity and was located at a depth of $\sim$20 km, in the down-dip beneath the hypocenter. It had a large slip zone, which extended to the western portion of the fault plane, resulting in a size of $\sim$10 $\times$ 15 km^2 that was dominated by left-lateral strike-slip movement. The maximum slip on this asperity was 120.2 cm. Asperity II appeared to be an isolated slip patch that developed in the shallower portion of the fault plane on the west side of the epicenter. Compared to the asperity I, the slip in this area was smaller ($\sim$50 cm) and occurred at shallower depths ($\sim$15 km). The slip in asperity II showed a left-lateral with small thrust movement. Some slips were also observed between asperity II and the epicenter but had smaller amounts of slip. It is worth noting that the aftershock distribution matches the edge of the main rupture zone. The average slip on the fault plane was $\sim$38.4 cm. Assuming a representative circular fault model, the average stress drop of the Meinong earthquake was 2.49 MPa.

Snapshots of the rupture process are shown in Figure 2a. In the first 2 s, the slip that ruptured in and around the hypocenter was very small. After the third second, a large slip ($\sim$30 cm) began to rupture beneath the hypocenter. In the time window between the third and eighth seconds, a large slip developed in the down-dip areas and propagated toward the west. This rupture behavior then immediately propagated through a large slip zone and formed asperity I. At $\sim$9 s, more slips began to occur at the shallow western area of the hypocenter. An isolated slip patch also occurred to the right of the hypocenter at approximately the fourth second. This slip patch continued developing until the end of the rupture at approximately the 16th second, and gradually formed asperity II on the fault plane. A constant rupture velocity ($V_r = 2.8$ km/s) is shown as a reference rupture front in Figure 2a. Most of the slips occurred after the reference rupture front had passed, especially the slip in the shallow asperity (asperity II). This indicates that the V_r at asperity II was relatively slow ($<$2.8 km/s). However, some slips during the development of Asperity I occurred before the reference rupture front from approximately the third to the sixth seconds. The average shear-wave velocity determined from a 3D tomography model (Huang *et al.*, 2014) in this area was about 3.23 km/s. This implies that the rupture speed during the development of asperity I was relatively fast, with a higher than average rupture velocity value (average V_r is about 0.8 times the shear-wavespeed).

The seismic moment release of the Meinong event was complex (Fig. 2b), containing several energy bursts during
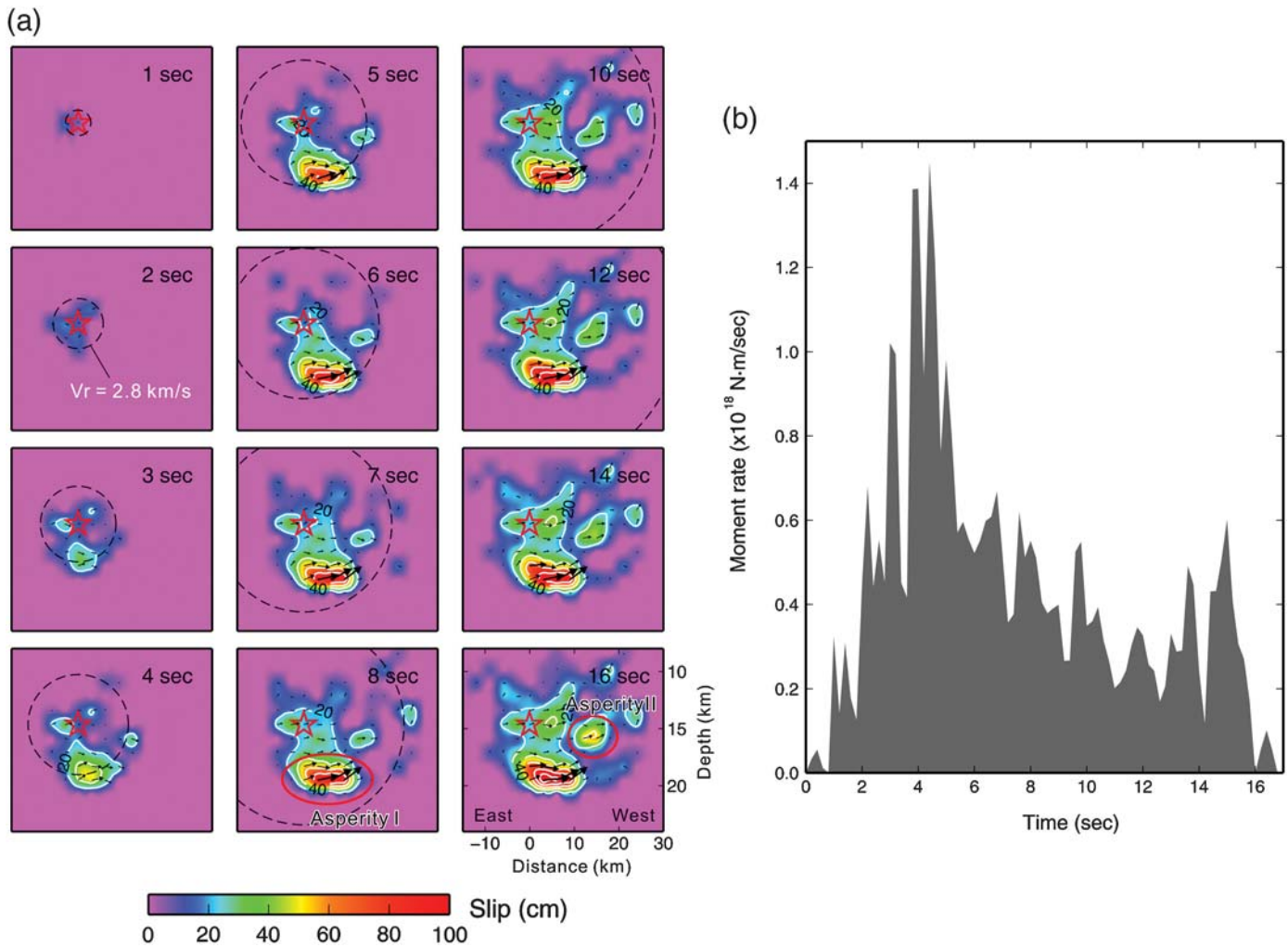
▲ **Figure 2.** (a) Snapshots of cumulative slip. The dashed open circle indicates a reference rupture front ($V_r = 2.8$ km/s). The star indicates the hypocenter as reported by CWB. Vectors are the slip direction and the amount of cumulative slip on each subfault. (b) Moment rate function of the Meinong earthquake.

rupture. The moment released at the beginning (0–2 s) was very small, followed by a series of large peak moment releases between the second and eighth seconds, which were related to the development of asperity I. During this time period (2–8 s), the rupture developed in the down-dip area and propagated in a westerly direction, releasing > 60% of the total moment. This represented the main rupture characteristic of the Meinong earthquake. Moments released after the eighth second were mainly due to the rupture that developed in the shallow fault plane. A small peak, occurring ~13–16 s, was caused by the growth of asperity II. The entire duration of the Meinong earthquake was ~16 s, and the total seismic moment release was 7.53×10^{18} N·m, equivalent to an earthquake of M_w 6.52.

FORWARD GROUND-MOTION SIMULATION

We adopted the inverted source rupture model to simulate the 3D wave propagation based on the SEM. The same SEM mesh model was used in the forward simulation study to ensure that

the path effect was identical in the inversion and forward processes. Because of the resolution limit of the 3D tomography model, the 3D wavefield and synthetic waveforms were simulated to 0.625 Hz. Ⓔ Movie S1 displays the simulated velocity wavefield for the east–west component. Because of the development of the fault rupture, a large number of seismic waves were generated from the source area in the first 20 s. After 20 s, the rupture on the fault plane stopped. However, because of the westward rupture, a strong directivity effect was observed to the west of the epicenter. Several series of strong, high-amplitude shakings, lasting for more than 30 s, spread into Tainan, Chiayi, and Kaohsiung. These strong seismic waves propagated all the way to the northwest and then gradually subsided when they reached northern Taiwan. In contrast to the strong shaking seen in the areas to the west of the epicenter, ground motion in eastern and southern Taiwan was relatively small.

We further analyzed the synthetic waveform calculated from the forward ground-motion simulation. The forward synthetic waveforms were compared with local ground-motion data
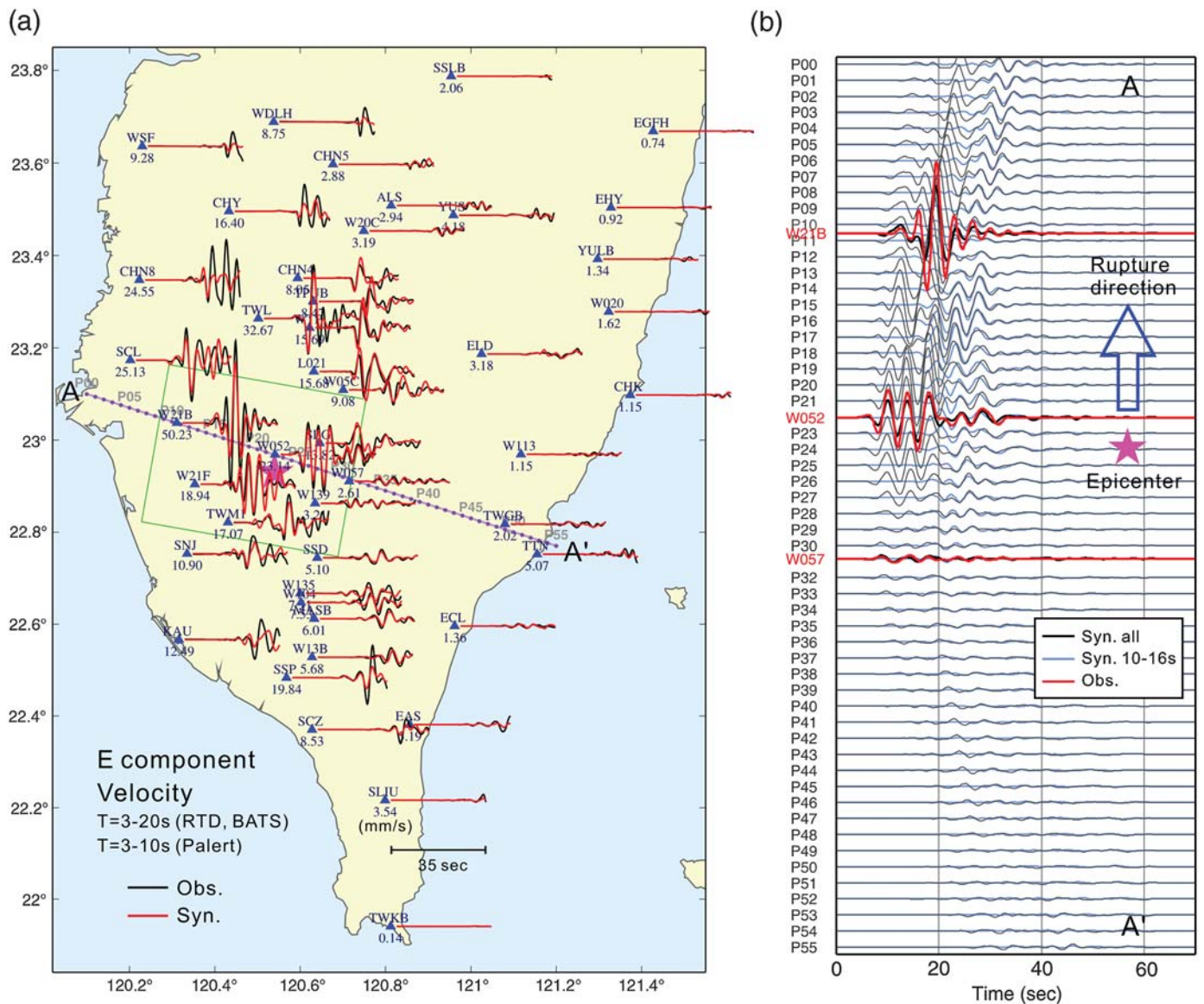
▲ **Figure 3.** (a) Comparison between local ground-motion records and forward synthetics for the east–west-component velocity waveforms. The CWB 24-bit and Broadband Array in Taiwan for Seismology waveforms were band-pass filtered between 0.05 and 0.33 Hz. The *P*alert data were filtered between 0.10 and 0.33 Hz. The maximum observed ground velocity is shown at the beginning of each waveform. (b) Comparison between *P*alert records and forward synthetic waveforms for the east–west component along A–A′ pseudostation array. Black lines are forward synthetics with full rupture process. Blue lines are synthetics with only 10–16 s rupture. Red lines are observations. Because of strong site effect, the amplitudes of SCL, W21B, and W21F were multiplied by 0.25, 0.20, and 0.25 to compare with the synthetics.

(Fig. 3a). Results show that the characteristics of the east–west component synthetic waveforms were similar to those observations in the period between 3 and 20 s (3 and 10 s for the *P*alert data). However, because the numerical simulation was not capable of completely reproducing the site amplification, the observed amplitudes at stations SCL, W21B, and W21F were respectively multiplied by a factor of 0.25, 0.2, and 0.25, so that they could be compared with the synthetic waveforms. The waveforms recorded in the Tainan area were generally characterized by a moderately large amplitude wave followed by a series of strong

amplitudes. Parts of these large amplitudes were more than 20 times larger than the waveforms recorded in the southern and eastern stations. The low-velocity structures that cannot be completely explained by the recent tomographic model may play important roles in amplifying the ground shaking in these specific areas. The overall misfit of the forward synthetic waveform is 0.37. With the details of the source rupture models and the 3D velocity model, we can closely reproduce the characteristics of the long-period strong ground motions of the Meinong earthquake for simulations accurate to a period of ∼3 s.
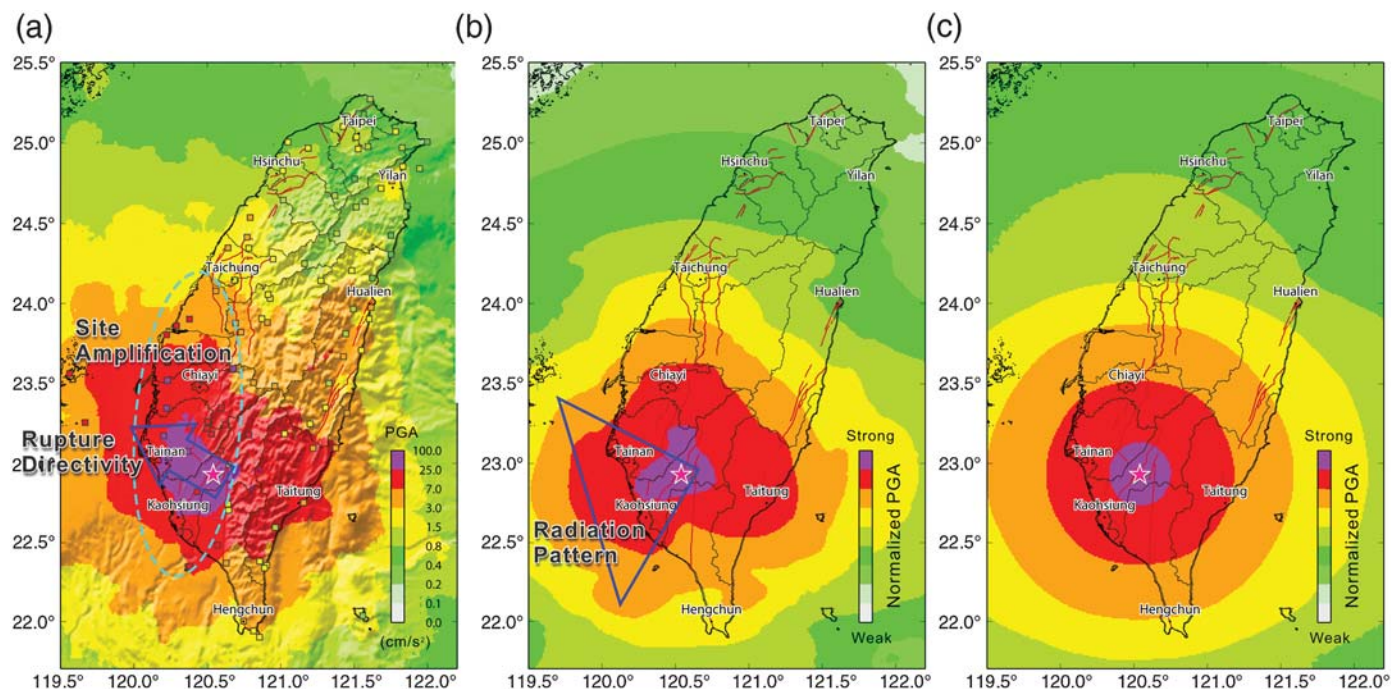
▲ **Figure 4.** The ShakeMaps (norm of the three-component peak ground acceleration [PGA]) determined from three different simulation cases: (a) a full 3D velocity and topography model with an inverted finite-fault source model, (b) a homogeneous half-space model (flat surface) with a double-couple point source, and (c) a homogeneous half-space model (flat surface) with an explosive source. The colored squares in (a) indicate the norm of PGA observations which were compiled from the CWB 24-bit Seismic Monitoring Network. The observations were low-pass filtered using a corner frequency of 0.625 Hz to compare with the simulated ShakeMap determined by a frequency of ≤0.625 Hz.

To investigate how the strong-motion waveform developed from the source area and was propagated into Tainan, synthetic waveforms along a pseudostation A–A′ array in a northwest–southeast direction were further analyzed. Figure 3b shows the east–west-component synthetic waveforms and strong-motion records near the array. The amplitude of the waveforms tended to be largest in the east–west component during the earthquake, especially in the Tainan area. The waveform amplitude for the station along the pseudoarray varied greatly by a factor of ~40, from 3.27 cm/s on the northwest side (P10) close to Tainan City, to 0.08 cm/s in the southeast station (P50). A remarkably strong velocity pulse originating from the epicenter and propagating into the Tainan area was observed. This velocity pulse had an extremely large amplitude with a relatively long duration that dominated the waveforms in all stations northwest of the epicenter. This phase commenced with the rupture of asperity I, which propagated in a northwesterly direction with a relatively fast rupture speed and resulted in an extremely strong rupture directivity effect in and along the rupture direction. This kind of velocity pulse, also called a killer pulse in earthquake engineering (Heaton *et al.*, 1995), contains huge amounts of kinetic energy that can cause serious damage to buildings. It is very likely that the collapse of the high-rise building and much of the other structural damage in the Tainan area was, to some extent, caused by this devastating killer pulse. The asperity II rupture mainly occurred 10 s after the rupture initiation. To demonstrate how asperity II

contributed to waveforms, we calculated the synthetic waveforms specifically for the period of 10–16 s after the initiation of the source time function. It is easier to identify the contributions through time and space by showing a pseudoarray, which is provided in Figure 3b. It shows that the contribution of asperity II was almost associated with the later phases. Indeed, these later phases extended the duration of ground shaking, whereas asperity II may contribute less to the peak ground motion in the Tainan and Chiayi areas.

DISCUSSION

We compared the observed PGA and the simulated ShakeMaps shown in Figure 4a. In this comparison, the CWB 24-bit data were used. A low-pass filter using a corner of 0.625 Hz was applied to the data so that it could be compared with the simulated ShakeMap with the same frequency band. The PGAs observed near the epicenter and the Tainan area were large. A strong PGA also extended northwestward into the Western Plain; however, it subsided quickly in northern Taiwan. Numerical simulation results further showed amplification of the PGAs in the Taiwan Strait, where a large PGA was observed on the Penghu Islands. All of the characteristics in the observed PGA were generally reproduced by the simulation. For the area to the east of the hypocenter, simulated PGAs were larger than those observed. Wang *et al.* (2010) proposed a 3D Q_P and Q_S tomography model beneath Taiwan. A low Q region can be

found beneath the Central Range in the 3D model. This high-attenuation feature has not been considered in the SEM mesh model. This may explain the greater amplitudes of the waves propagating from the Meinong source region toward eastern Taiwan.

To determine the main factors that caused the amplification of ground shaking in southern Taiwan, we considered three different source models in the SEM simulations: finite-fault, point double-couple, and explosive. The ShakeMaps of the three source models are shown in Figure 4. In the explosive source model (Fig. 4c), a concentric circular ShakeMap distribution, centered on the epicenter, was shown as expected. The result derived from the point double-couple source model (Fig. 4b) showed strong ground motion on the west and east sides of the epicenter but especially in the western areas where the cities of Tainan and Kaohsiung are located. This phenomenon is due to source radiation that causes amplified ground motion in specific positions. The ShakeMap pattern resulting from the finite-fault rupture model is complex. The PGA shows large amplifications not only on the west side of the source area but also extending in a northwest direction (Fig. 4a). As we discovered from the source inversion result, the rupture of the Meinong earthquake occurred mainly from the southeast from the epicenter and extended toward the northwest. This rupture characteristic can cause a strong directivity effect that amplifies the ground motion in the Tainan area. In addition, the simulation result shows amplifications in most areas of western Taiwan. This result reflects the fact that the seismic wave propagated through the Western Plain, which is made up of thick, low velocity, sedimentary deposits. Although the simulation performed in this study is considered accurate in the low-frequency range (e.g., 0.33 Hz), we noticed that the amplification could not be reproduced adequately at some stations because of the sedimentary layer near the surface. Because we have already considered rupture directivity, radiation pattern, and 3D velocity structure, it is reasonable to conclude that the underestimated amplitudes are attributed to the site or nonlinear near-surface amplifications. Consequently, the factors that we used for amplification corrections at stations SCL, W21B, and W21F serve as estimations of the near-surface amplification in this frequency range. A comparison between simulations with and without surface topography is shown in Ⓔ Figure S7. The topography amplified the PGA in parts of the mountainous area. However, the anomalously large ground motion observed in western Taiwan, that is, the Tainan and Chiayi areas, was not significantly influenced by the topography in the 3–20 s period. From the results of these numerical simulations, we concluded that the anomalously large ground motion in Tainan during the Meinong earthquake was caused by an accumulative effect of three factors: (1) rupture directivity, (2) source radiation pattern, and (3) sedimentary amplification.

CONCLUSIONS

The joint source inversion result of the Meinong earthquake indicates that the spatial extent of the rupture area was $\sim 25 \times 25$ km^2, and the maximum slip was larger than 1 m. The rupture was complex and included at least two asperities on the fault plane. In the first 8 s, asperity I developed in the down-dip area below the hypocenter and caused the rupture to propagate toward the northwest with V_r higher than 0.8 V_S. Asperity II was located in the shallow part that slipped for a long time from the fourth second until the end of the rupture. In the 3D wave propagation simulation, we demonstrated that the strong ground shaking observed in Tainan could be reproduced by three factors: (a) rupture directivity, (b) source radiation pattern, and (c) sedimentary amplification. The numerical earthquake model of the Meinong earthquake presented here suggests that the northwest-striking blind fault in southern Taiwan can cause serious seismic hazards, especially in the areas of Tainan and Chiayi. This event is also an example of how a moderate earthquake can produce anomalously strong ground motion in regions with similar geological characteristics.

DATA AND RESOURCES

ACKNOWLEDGMENTS

REFERENCES

Ching, K. E., K. M. Johnson, R. J. Rau, R. Y. Chuang, L. C. Kuo, and P. L. Leu (2011). Inferred fault geometry and slip distribution of the 2010 Jiashian, Taiwan, earthquake is consistent with a thick-skinned deformation model, *Earth Planet. Sci. Lett.* **301**, nos. 1/2, 78–86.

Deffontaines, B., O. Lacombe, J. Angelier, H. T. Chu, F. Mouthereace, C. T. Lee, J. Deramond, J. F. Lee, M. S. Yu, and P. M. Liew (1997). Quaternary transfer faulting in Taiwan Foothills: Evidence from a multisource approach, *Tectonophysics* **274**, 61–82.

Dziewonski, A. M., T. A. Chou, and J. H. Woodhouse (1981). Determination of earthquake source parameters from waveform data for studies of global and regional seismicity, *J. Geophys. Res.* **86**, 2825–2852.

Hartzell, S. H., and T. H. Heaton (1983). Inversion of strong ground motion and teleseismic waveform data for the fault rupture history

of the 1979 Imperial Valley, California earthquake, *Bull. Seismol. Soc. Am.* **73,** 1553–1583.

Heaton, T. H., J. F. Hall, D. J. Wald, and M. W. Halling (1995). Response of high-rise and base-isolated buildings to hypothetical M_w 7.0 blind thrust earthquake, *Science* **267,** 206–211.

Huang, H. H., Y. M. Wu, T. L. Lin, W. A. Chao, J. B. H. Shyu, C. H. Chan, and C. H. Chang (2011). The preliminary study of the 4 March 2010 M_w 6.3 Jiasian, Taiwan, earthquake sequence, *Terr. Atmos. Ocean. Sci.* **22,** no. 3, 283–290.

Huang, H. H., Y. M. Wu, X. Song, C. H. Chang, S. J. Lee, T. M. Chang, and H. H. Hsieh (2014). Joint V_P and V_S tomography of Taiwan: Implications for subduction-collision orogeny, *Earth Planet. Sci. Lett.* **392,** 177–191.

Kikuchi, M., and H. Kanamori (1982). Inversion of complex body waves, *Bull. Seismol. Soc. Am.* **72,** no. 2, 491–506.

Komatitsch, D., and J. Tromp (1999). Introduction to the spectral-element method for 3-D seismic wave propagation, *Geophys. J. Int.* **139,** 806–822.

Komatitsch, D., Q. Liu, J. Tromp, P. Süss, C. Stidham, and J. H. Shaw (2004). Simulations of ground motion in the Los Angeles basin based upon the spectral-element method, *Bull. Seismol. Soc. Am.* **94,** 187–206.

Lacombe, O., F. Mouthereau, J. Angelier, and B. Deffontaines (2001). Structural, geodetic and seismological evidence for tectonic escape in SW Taiwan, *Tectonophysics* **333,** 323–345.

Lee, S. J., W. T. Liang, L. Mozziconacci, Y. J. Hsu, W. G. Huang, and B. S. Huang (2013). Source complexity of the 4 March 2010 Jiashian, Taiwan earthquake determined by joint inversion of teleseismic and near field data, *J. Asian Earth Sci.* **64,** 14–26.

Lee, S. J., K. F. Ma, and H. W. Chen (2006). Three-dimensional dense strong motion waveform inversion for the rupture process of the 1999 Chi-Chi, Taiwan, earthquake, *J. Geophys. Res.* **111,** no. B11, doi: 10.1029/2005JB004097.

Lin, P. S., C. T. Lee, C. T. Cheng, and C. H. Sung (2011). Response spectral attenuation relations for shallow crustal earthquakes in Taiwan, *Eng. Geol.* **121,** no. 3, 150–164.

Okada, Y. (1985). Surface deformation due to shear and tensile faults in a half-space, *Bull. Seismol. Soc. Am.* **83,** 1135–1154.

Wang, Y. J., K. F. Ma, F. Mouthereau, and D. Eberhart-Phillips (2010). Three-dimensional Q_P- and Q_S-tomography beneath Taiwan orogenic belt: Implications for tectonic and thermal structure, *Geophys. J. Int.* **180,** 891–910.

Wu, Y. M., D. Y. Chen, T. L. Lin, C. Y. Hsieh, T. L. Chin, W. Y. Chang, W. S. Li, and S. H. Ker (2013). A high-density seismic network for earthquake early warning in Taiwan based on low cost sensors, *Seismol. Res. Lett.* **84,** no. 6, 1048–1054.

Yen, T. P., and P. L. Tien (1986). Chaochou fault in southern Taiwan, *Proc. Geol. Soc. China* **29,** 9–22.

Shiann-Jong Lee
Te-Yang Yeh
Yen-Yu Lin
Institute of Earth Sciences
Academia Sinica
No. 128, Section 2
Academia Road, Nankang
Taipei 11529, Taiwan
sjlee@earth.sinica.edu.tw